Droplet Entrainment in Vertical Annular Flow and Its Contribution to Momentum Transfer

Simultaneous measurements were made of the size and the axial and radial velocity of drops entrained by the gas in annular flow. A model is developed to use these data to compute the rate of deposition or entrainment and the pressure gradient, ∇p_E, due to drop interchange. ∇p_E is a significant fraction of the measured total gradient, ∇p.

J. C. B. Lopes, A. E. Dukler
Department of Chemical Engineering
Cullen College of Engineering
University of Houston
Houston, TX 77004

SCOPE

Annular flow exists in a pipe whenever gas and liquid are flowing simultaneously with the gas phase moving at high speed. Drops of liquid are always entrained by the gas and the average volume fraction of the liquid is small. The observed pressure drops are substantially higher than values observed in single-phase pipe flow, as are the rates of heat and mass transfer.

Various attempts have been made to explain the observed high-pressure gradient in annular flow. In general the measured pressure gradient has been considered to be solely the result of shear due to the flow of gas over the wavy liquid interface (Wallis, 1968; Hughmark, 1972; Henstock and Hanratty, 1975; Barathan, 1978). But, in fact another mechanism exists for generating a pressure gradient: the dynamic interchange between liquid moving as entrained drops and the slow-moving liquid film on the wall. Dukler and Magiros (1962) and Moeck and Stochiewicz (1972) have explored this mechanism in a preliminary way.

It was the objective of this work to analyze this droplet interchange process, to quantitatively determine the deposition and entrainment rates, and to evaluate their contribution to the measured pressure gradient. Droplet interchange can provide another mechanism for the enhanced rate of heat and mass transfer observed in annular flow. Drops having a high surface-to-volume ratio interact with the gas where exchange can take place. They deposit in the liquid film and fresh drops enter the gas phase, thus transferring energy or mass in a type of renewal process. Modeling these transfer rates requires an understanding of the droplet exchange process.

Experiments on gas-liquid annular flow were carried out with air-water in a 0.051 m dia. vertical test section about 10 m long. Simultaneous measurements were made of size and axial and radial velocity of the entrained drops using a modification of a method introduced by Semiat and Dukler (1981). These data were used to determine the distribution of the drop trajectory angles and size distribution, from which deposition rates could be computed. This information along with measurements of total pressure gradient, ∇p, mean film thickness, $\bar{m}$, and rate of flow of entrained liquid, W_{LE}, permits a direct computation of the pressure gradient due to entrainment interchange, ∇p_E, gravity, ∇p_G, and interfacial shear ∇p_I, where $\nabla p = \nabla p_E + \nabla p_3 + \nabla p_I$. These computations were made over a range of gas and liquid rates characteristic of annular flow.

CONCLUSIONS AND SIGNIFICANCE

In annular flow, the entrainment and deposition of drops and the momentum exchange accompanying this process can account for a substantial part of the pressure gradient observed. Figure 20 displays the distribution of each of the pressure gradient contributions as they change with gas and liquid rate. At higher liquid rates ∇p_E can account for over half of the total ∇p. Attempts to correlate interfacial shear by methods sim-

The present address of J. C. B. Lopes is Schlumberger-Doll Research, Old Quarry Road, Ridgefield, CT 06887.

ilar to those used for single-phase flow ignore this mechanism.

From this work it is possible to compute the pressure gradient due to interfacial shear ∇p_I. As revealed in Figure 22, the usual friction factor method of coordinating this data shows a correlation independent of liquid rate with the features of a transition-type roughness.

The Linear Momentum Balance

Consider the following simplified picture of upward annular flow in a vertical column, Figure 1:

- A continuous liquid film flows over the inner surface with a mean film thickness $\overline{m}$ and flow rate W_{LF}.
- A continuous gas phase moves at a flow rate W_G, through a core of diameter $D_c = D - 2\overline{m}$, carrying dispersed liquid drops at a rate W_{LE}. In the gas core the void fraction is α_c.
- A gas-liquid interface separates the two continuous phases, through which liquid is interchanged in the form of droplets with a deposition mass flux, N_D, and entrainment flux, N_E. It will be assumed that equilibrium exists, i.e., $N_E = N_D$.

In particular, consider the control volume, V_C, of length L_D shown in Figure 1. Applying the Reynolds transport theorem for momentum transfer over the gas core region, V_C, enclosed by the area, S_C, results in the following equation of conservation of linear momentum where the process is assumed to be steady state on time average:

$$\iint_{S_C} \underline{T} dA + \iiint_{V_C} \underline{B}\rho dV = \iint_{S_C} \underline{v}(\rho \underline{v} \cdot d\underline{A}), \qquad (1)$$

where: $\underline{v}$ is the velocity vector; ρ is the local density; $d\underline{A}$ is an infinitesimal area element vector directed to the exterior of the closed surface, S_C; $\underline{B}$ is the local body force per unit mass vector; and $\underline{T}$ is the local traction vector acting on the surface S_C. The scalar component of this equation in the axial direction, z, can be obtained by taking the inner product of Eq. 1 with the unit vector $\underline{k}$ in the z direction.

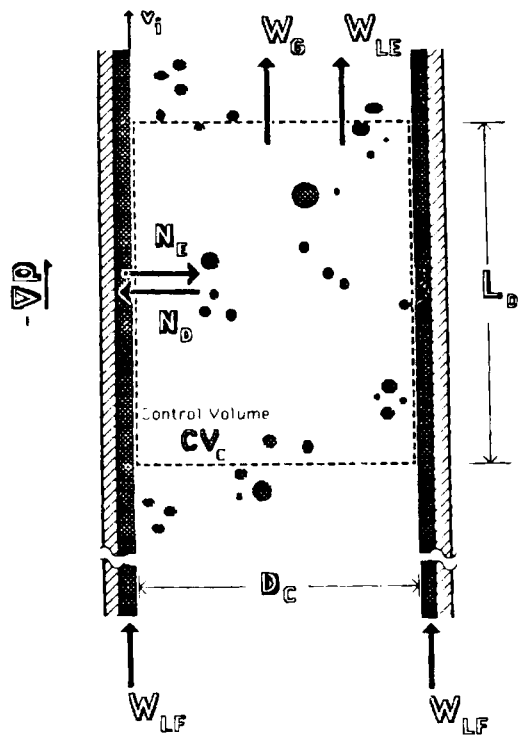

Figure 1. Control volume description for momentum balance in annular flow.

The body force acting in the z direction is $B_z = -g$, where g is the acceleration of gravity. The control volume, V_C, can be partitioned into the liquid and gas volumes V_L and V_G to give:

$$\iiint_{V_C} B_z \rho dV = \iiint_{V_L} -g\rho_l dV + \iiint_{V_G} -g\rho_g dV. \qquad (2)$$

Assuming the gas density constant within the control volume and designating α_c as the void fraction in the gas core results in:

$$\iiint_{V_C} B_z \rho dV = -g[(1-\alpha_c)\rho_l + \alpha_c \rho_g] \frac{\pi D_c^2}{4} L_D. \qquad (3)$$

In a similar way the surface force term can be partitioned into the interfacial surface, S_L, where the interfacial shear $-\tau_i$ acts, and the two transverse areas, S_T, where only the normal pressure p acts:

$$\iint_{S_C} T_z dA = \iint_{S_L} -\tau_i dA + \iint_{S_T} p dA$$
$$= -\tau_i \pi D_C L_D + \Delta p \frac{\pi D_c^2}{4}, \qquad (4)$$

where, Δp is the pressure difference between two axial points separated by a distance L_D.

The convective term can also be considered in two parts: the net momentum flux through the ends and the net momentum flux through the interface. The first term has a zero contribution since steady incompressible parallel flow is assumed. Furthermore, there is no gas flow through the lateral area, hence the remaining term contains only the z-momentum flux contribution of the droplets being deposited and entrained. Assuming that the droplets deposit at a mass flux rate, N_D, having an average axial velocity, $\overline{v}_z$, and are entrained at a mass flux rate, N_E, carrying the axial velocity of the moving interface, v_i, then:

$$\iint_{S_C} v_z(\rho \underline{v} \cdot d\underline{A}) = (\pi D_c L_D)(N_D \overline{v}_z - N_E v_i). \qquad (5)$$

Inserting Eqs. 3, 4, and 5 into Eq. 1 and setting $N_E = N_D$, results after some manipulation in:

$$\frac{\Delta p}{L_D} = \frac{4\tau_i}{D_C} + g[\alpha_c \rho_g + (1-\alpha_c)\rho_l] + \frac{4}{D_C} N_D(\overline{v}_z - v_i). \qquad (6)$$

From this equation, the total pressure gradient, $\nabla p = \Delta_p / L_D$, can be thought of as the sum of three pressure gradient terms:

$$\nabla p = \nabla p_I + \nabla p_G + \nabla p_E, \qquad (7)$$

where:

• ∇p_I is the interfacial pressure gradient due the gradient shear of the gas at the interface and

$$\nabla p_I = \frac{4\tau_i}{D_C}. \tag{8}$$

• ∇p_G is the gravitational pressure gradient and

$$\nabla p_G = g[\alpha_c \rho_g + (1 - \alpha_c)\rho_l]. \tag{9}$$

∇p_E is the entrainment pressure gradient resulting from the net acceleration of liquid from a slow-moving film to a fast-moving droplet, and

$$\nabla p_E = \frac{4}{D_C} N_D(\bar{v}_z - v_i). \tag{10}$$

It is the objective of this study to determine the values of ∇p_I. It will be shown in what follows that ∇p, ∇p_G, and ∇p_E can be obtained from measurements of the axial and radial velocities of the drops, the total pressure gradient, the liquid rates W_{LE} and W_{LF}, and the average liquid thickness $\bar{m}$.

The gas core void fraction, α_c, can be obtained given measurements of W_{LE} and $\bar{v}_z$ through the relationship:

$$W_{LE} = \rho_l(1 - \alpha_c)A_c\bar{v}_z. \tag{11}$$

This permits ∇p_G to be calculated through Eq. 9. N_D and v_i are required in Eq. 10 to calculate ∇p_E. The interfacial velocity can be estimated by assuming a linear velocity profile exists in the film. Then:

$$v_i = 2U_{LF} = \frac{2(W_L - W_{LE})}{\pi\rho_l\bar{m}(D - \bar{m})}, \tag{12}$$

where U_{LF} is the mean liquid velocity in the film and W_L is the total liquid rate in the pipe. It remains to determine N_D, and this will be developed in a following section.

Experimental

The flow loop used in this work is represented schematically in Figure 2. The test section consists of a 10 m long vertical Plexiglas column with an internal diameter of 50.74 ± 0.18 mm and a nominal wall thickness of 6.4 mm. The fluids used, air and water, were injected at the bottom of the column using the entry devices shown in Figures 2b and 2c. The air was injected radially and passed through a calming section with a length equivalent to 17.5 column diameters. Then the water was injected axially through an annulus around the inside pipe wall. This design was developed to minimize the entrance effects. When the fluids contacted, they were already moving at the prevailing directions and velocities in annular flow, and equilibrium annular flow was attained in a very short distance. This type of injection also avoids the creation of very fine droplet sprays.

The experimental measurements of droplet sizes and velocities were made at 8.9 m from the gas injection point, equivalent to a distance of 175 pipe diameters. Both temperature and pressure were monitored at the measuring location and experiments were run at superficial velocities in the ranges 14–25 m/s for the gas and 0.03–0.12 m/s for the liquid.

Measurement of drop size and velocity

The basic optical technique for simultaneous measurement of drop size and velocity is described in a paper by Semiat and Dukler (1981) where the principles of the method are developed. Droplets in annular flow are moving at relatively high velocities (from 5 to 30 m/s) and have a wide spectrum of sizes (100 μm to 3 mm). In addition, the presence of a wavy liquid film on the internal wall of the pipe presents special problems for optical access. These characteristics required the development of special optical techniques and a data acquisition system capable of processing the fast transit time of the drops.

A 1,200 μm dia. beam from a 15 mW He-Ne laser, Spectra-Physics model 124–A, was introduced by means of a 3,000 μm dia., 4 cm long quartz rod with flat polished ends, as shown in Figure 3. The rod was positioned to allow a clearance of 7,500 μm from the intended point of droplet measurements. The first measuring point was located just in front of the incident beam. Light intensity was measured through a 75 × 2,000 μm rectangular slit positioned normal to the direction of the gas flow. The light passing through this slit was carried by an optic fiber ribbon to photomultiplier *PM1*.

The second measuring point was positioned at a 38° angle to the horizontal incident beam. Light was measured through a 800 μm pinhole. A cylindrical optic fiber recessed in a hollow metallic tube supporting the pinhole carried the light to photomultiplier *PM2*. This special arrangement resulted in a measuring volume with an elliptic cross section with principal axis dimensions of 1,100 × 1,786 μm and 75 μm thick, enabling local measurements. Only particles passing through this region could be detected simultaneously by *PM1* and *PM2*. Semiat and Dukler showed that the existence of a simultaneous signal assured the measurement of the drop diameter rather than a chord. Data were obtained at three different radial positions by installing three sets of quartz rods and translating the optics arrangement, as shown in Figure 3b.

Before the laser beam passes into the test section it crossed two successive Ronchi gratings, each having a fringe spacing, s_F = 50 μm. One grating created a series of fringes oriented horizontally inside the laser beam traveling upward and the second a set of vertical fringes moving radially. The disks supporting the Ronchi gratings were rotated by two adjustable constant speed motors set to generate light frequencies on a fixed object at the measuring point of 1.0 MHz, as a result of the vertical translation of the horizontal fringes, and 0.6 MHz, due to radial translation of the vertical fringes. A particle moving through the measuring point with axial velocity v_z and radial velocity v_y will display two frequencies as follows:

$$f_z[\text{MHz}] = 1.0 + \frac{v_z}{s_F}, \tag{13}$$

and

$$f_y[\text{MHz}] = 0.6 + \frac{v_y}{s_F}, \tag{14}$$

The light intensity fluctuation is detected by *PM2*, the two frequencies are separated by band-pass filtering, and the frequencies are measured using TSI model 1990 frequency counters Then v_z and v_y can be determined from Eqs. 13 and 14. The drop diameter, d, is determined from the time required for the drop to

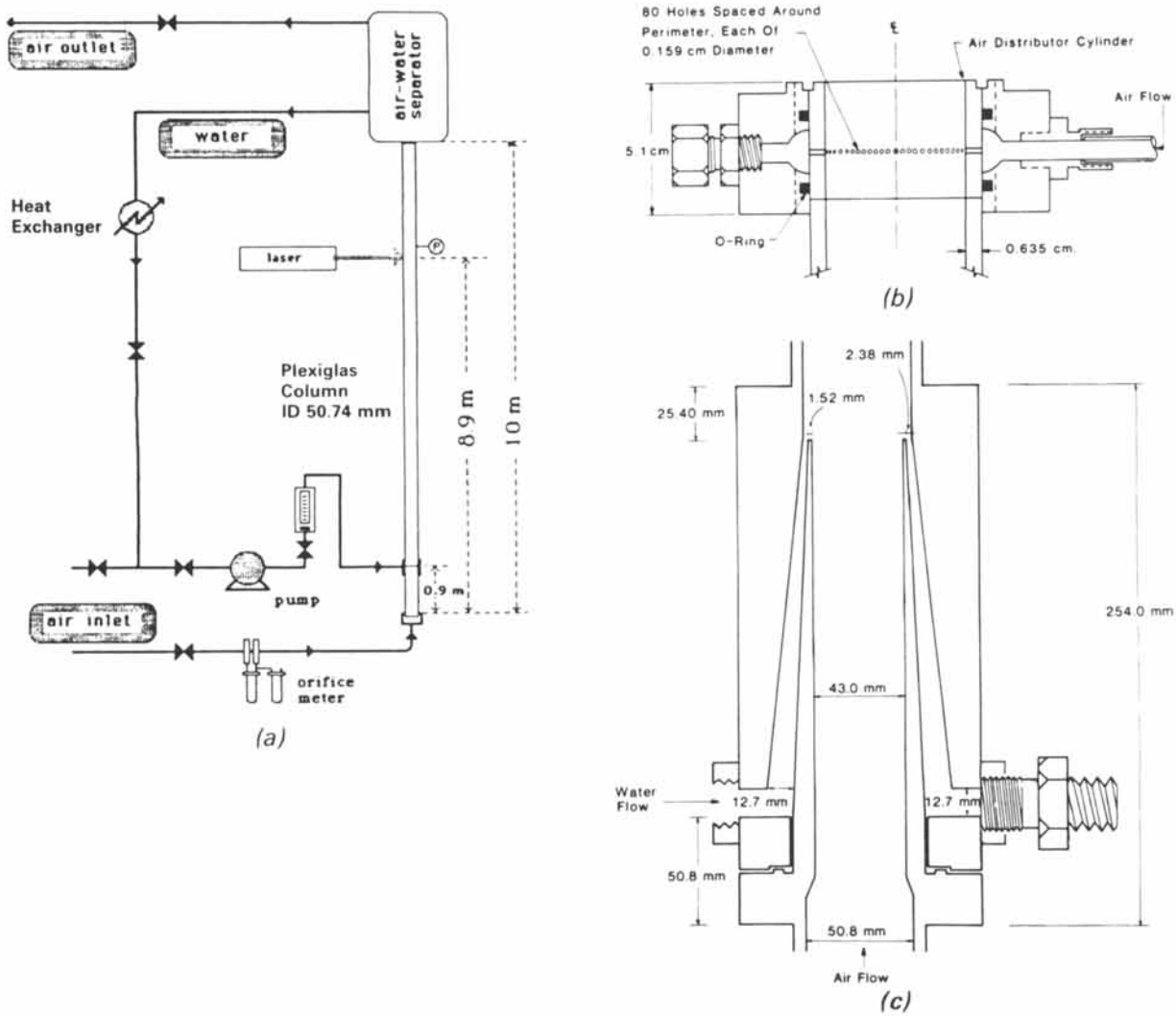

Figure 2. Experimental apparatus.

a. Vertical multiphase flow loop
b. Gas injection device
c. Liquid injection device

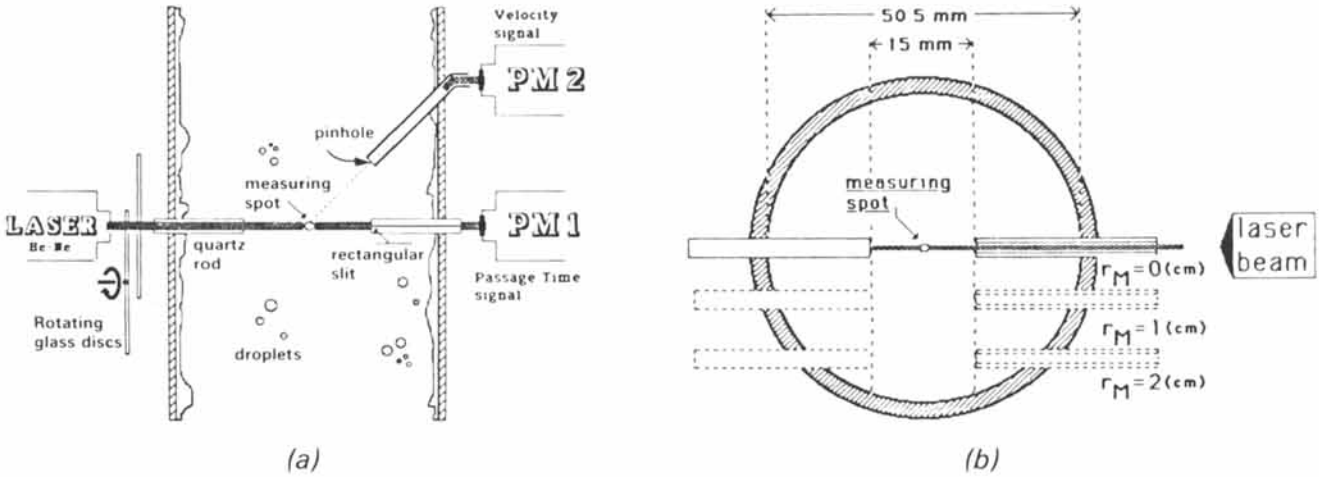

Figure 3. Spatial configuration of laser and light intensity measuring points at test section.

a. Vertical cut
b. Transverse cut

pass across the slit located in front of *PM1*. This passage time, τ_{PT}, is obtained by measuring the time that the light is deflected as the drops move through the measuring spot. Then:

$$\tau_{PT} = \frac{d + s}{v_z}, \tag{15}$$

where s is the slit gap size in the axial direction.

A detailed analysis of the optical method for this application was presented by Lopes (1984) along with a model for the interaction of multiple drops with the laser beam. This analysis makes possible the interpretation of the signals generated by *PM1* and *PM2* and the automatic processing of the signals, as shown in Figure 4.

Typical Experimental Results

Drop size distributions

Figure 5 shows the number-diameter and volume-diameter probability distributions, F_d^N and F_d^V, respectively, at centerline for the four extreme liquid and gas rate combinations. $F_d^N(d)$ is the number fraction of drops having a diameter less than d, and $F_d^V(d)$ is the corresponding volume fraction. A comparison between the number and volume distributions clearly shows that despite the fact that the smaller sizes dominate in numbers in all the cases, the larger sizes carry most of the volume. For instance, in the case of U_{GS} = 24.5 m/s and U_{LS} = 0.121 m/s, 50% of the drops below the mean diameter represented less than 10% of the volume, while 50% of the volume above the mean represented less than 10% of the drop count. This observation

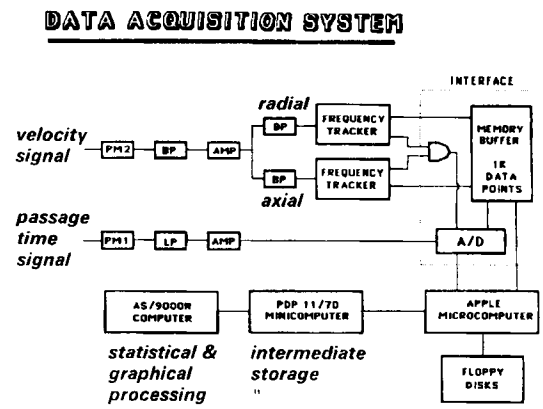

PM - Photomultiplier
BP - Band Pass Filter
LP - Low Pass Filter
AMP - Amplifier
A/D - Analog to Digital Converter

Figure 4. Data acquisition system diagram for droplet size and two velocity component measurements.

stresses the importance of the large drops in processes of momentum and mass transfer. The change in the F_d^N curves with increasing U_{GS} results from the fragmentation of the larger droplets with increasing gas rates. The drop size statistics showed a strong dependence on U_{GS}, as is illustrated in Figure 6 for the mean Sauter diameter, $\bar{d}_{32}$, and the maximum detected

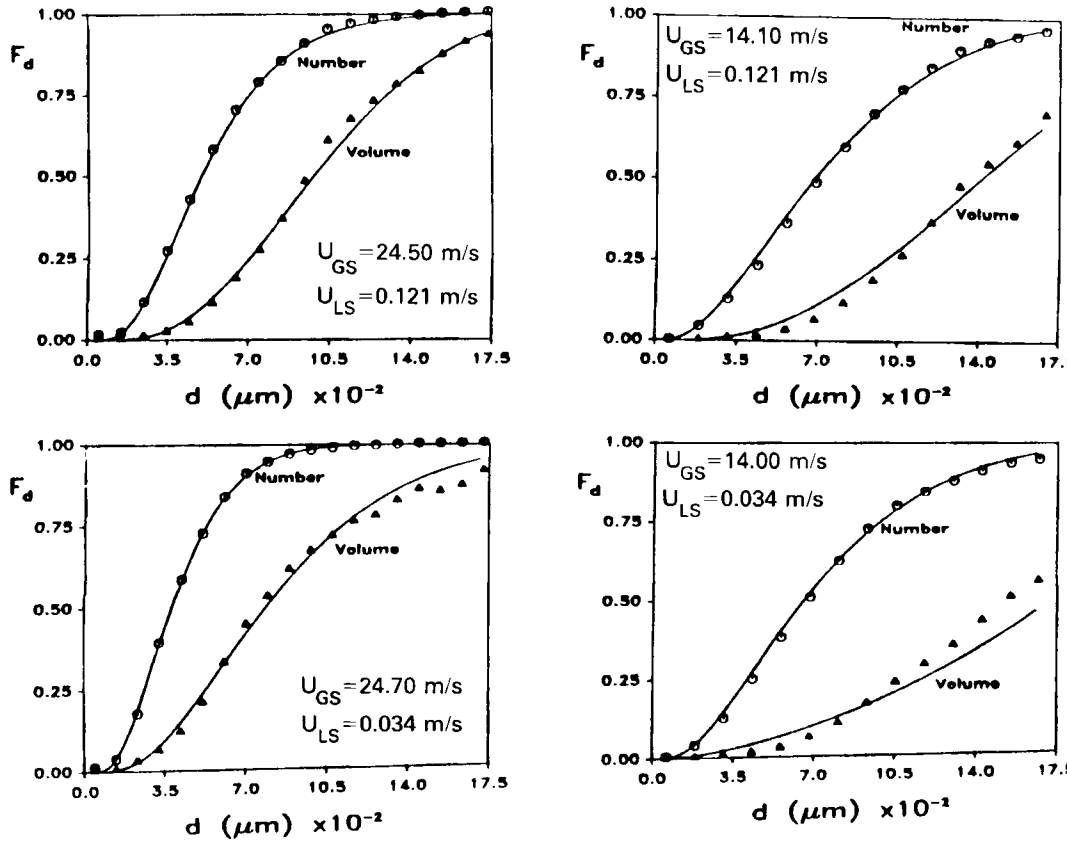

Figure 5. Number- and volume-based drop diameter distribution functions at centerline.

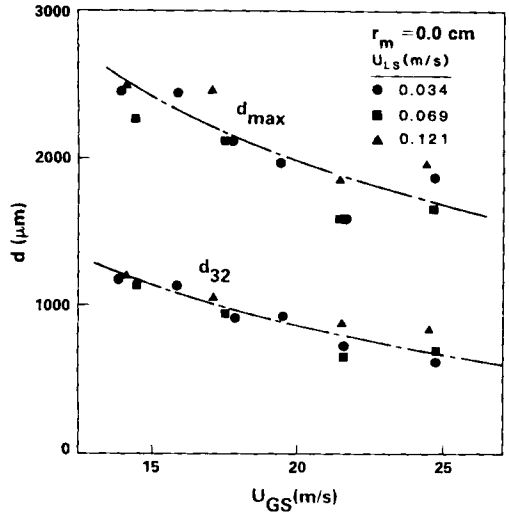

Figure 6. Dependence of mean drop diameter $\bar{d}_{32}$ and maximum detected drop diameter on flow rates at centerline.

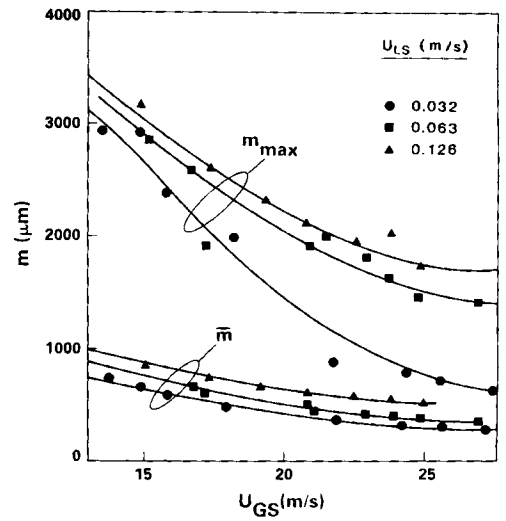

Figure 7. Mean and maximum film thicknesses vs. superficial gas velocity (Zabaras, 1985).

drop diameter, d_{max} at the centerline position. The dependence on liquid rates seems to be small.

It is of interest to compare these results with the statistics on film thickness in vertical upward annular flow, since all the droplets originated from the liquid film. In Figure 7 the results of Zabaras (1985) are presented for average film thickness, $\bar{m}$, and maximum film thickness, m_{max}, taken in equipment similar to that used in this work. A strong dependence of m_{max} on both gas and liquid rates were found. This contrasts with the independence of $\bar{d}_{32}$ and d_{max} on liquid rates, which is an indication that the mean drop size and d_{max} are mainly determined by the interactions of the droplets with the carrier gas, rather than depending on the size of the liquid film from which it originated.

The Sauter mean diameters reported here are substantially larger than those indicated by Azzopardi (1985). The difference is due largely to the fact that $\bar{d}_{32}$ is very sensitive to the existence of large sizes and the experimental method used by Azzopardi is unable to reliably detect drop sizes above 500 μm (Swithenbank et al., 1977). In addition, the larger gas velocities in his experiments result in smaller drop sizes.

Axial velocity of droplets

Typical probability density data for the axial velocities as measured at the centerline are presented in Figure 8. The solid curves represent the best fit using a Gaussian model. Mean values of the axial velocity, $\bar{v}_z$, appear in Figure 9 where it is seen that $\bar{v}_z$ is only weakly dependent on liquid rate.

A quantity of some importance is the slip velocity, $U_S = U_G - \bar{v}_z$, and the slip ratio, S_R, defined as:

$$S_R = \frac{U_S}{U_G}. \tag{16}$$

While the local gas velocity was not measured in this study, its value at the axis, U_{G_0}, can be estimated from the universal veloc-

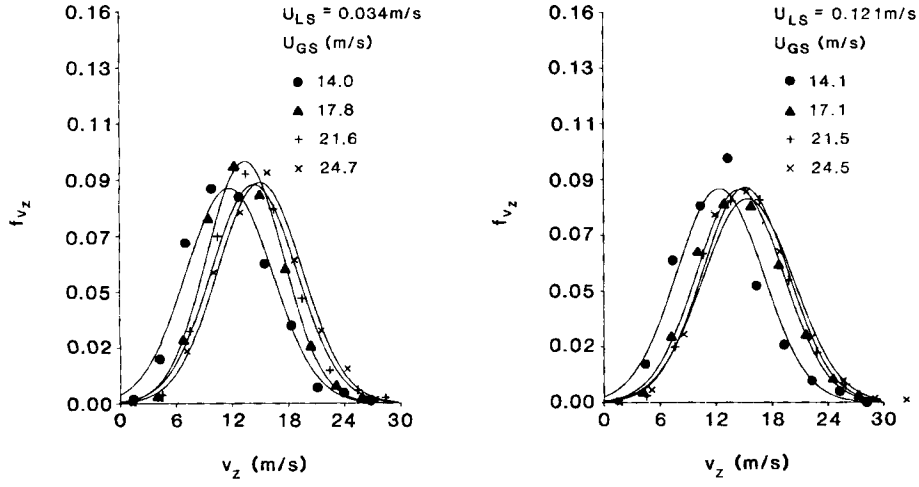

Figure 8. Dependence of droplet axial velocity p.d.f. (probability density function) on gas rates for different liquid rates at centerline.

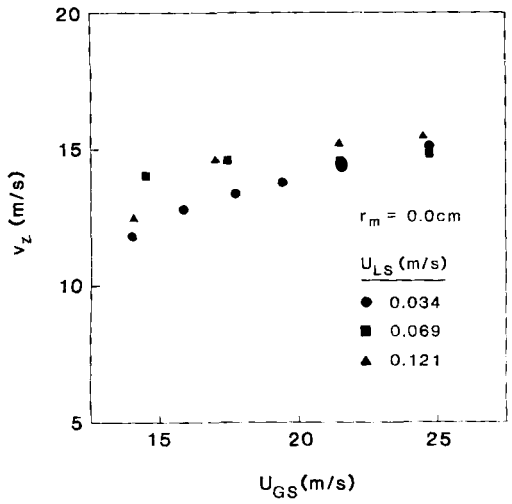

Figure 9. Dependence of droplet average velocity $\bar{v}_z$ on gas flow rate at centerline.

ity distribution law discussed by Schlichting (1979):

$$U_{G_0} = 3.75u^* + U_{GS}, \tag{17}$$

where u^* is the gas friction velocity. This relationship is shown by Schlichting to be equally valid for smooth and rough pipes. The average slip velocity at the centerline, U_{S_0}, can be found from:

$$U_{S_0} = U_{GS} + 3.75u^* - \bar{v}_{z_0}, \tag{18}$$

and the corresponding slip ratio by:

$$S_{R_0} = 1 - \frac{\bar{v}_{z_0}}{U_{GS} + 3.75u^*}. \tag{19}$$

For each experimental point, the calculated values of interfacial shear and measured gas density were used to compute u^* and Eq. 19 was used to find S_{R_0}. The results, which appear in Figure 10, again show an insensitivity to liquid rate. Of importance is the fact that the slip is of the order of 50% of the gas rate, much larger than previously thought to exist.

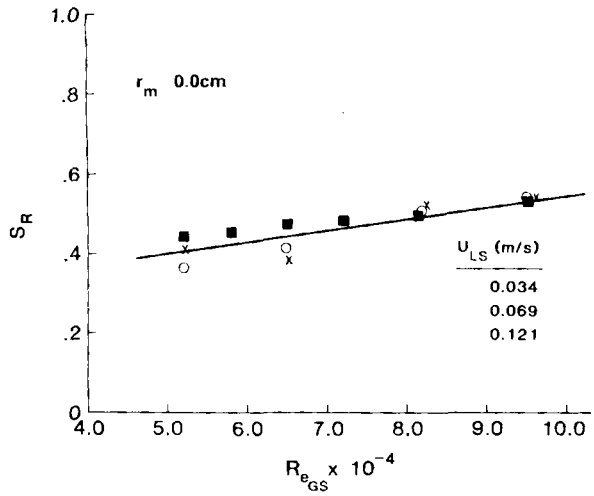

Figure 10. Experimental slip ratio vs. gas Reynolds number at centerline.

Lateral velocity of droplets

An estimation of the radial velocity can be obtained from the average value of the absolute lateral velocity $|\overline{v_y}|$. Values of $|\overline{v_y}|$ are plotted in Figure 11 vs. the gas Reynolds number, Re_{GS}, for all the radial positions. Note that $|\overline{v_y}|$ is nearly independent of liquid and gas rate and has a value independent of radial position as well.

Andreussi and Azzopardi (1983), following a suggestion made by Tatterson (1975), speculated that the kinetic energy of the droplet is proportional to the work done by the gas pressure forces on the wave as the drop is formed. The result is that $|\overline{v_y}|$ is proportional to the friction velocity u^*. This was confirmed by Wilkes *et al.* (1983) working with a different pipe size. Although the proportionality constant was different, $|\overline{v_y}|$ was also proportional to u^*. In the study reported here the values of u^* based on the interfacial shear and measured gas density were shown to vary over the narrow range of 1.9 to 2.0 m/s for the full range of gas and liquid rates reported. Thus the constancy of $|\overline{v_y}|$ is consistent with earlier work.

Simultaneous measurements of lateral and axial velocity makes it possible to calculate the angle each drop makes with the axis, and from an array of such measurements statistics can be calculated. The angle θ can be defined as:

$$\theta = \frac{\pi}{2} - \left|\arctan\left(\frac{v_z}{v_y}\right)\right|, \quad 0 \le \theta \le \frac{\pi}{2}, \tag{20}$$

and if the volume for each drop is known, then the experimental volume-angle probability density functions for the angle, f_θ^V, can be determined from $f_\theta^V = dV(\theta)/d\theta$ where $V(\theta)$ is the volume fraction of the drops with angle θ. Figure 12 shows the experimental volume-angle probability density functions for the angle f_θ^V taken at the tube axis. The mean values, $\bar{\theta}_V$, in Figure 13 show the existence of a remarkably constant mean value, θ_V =

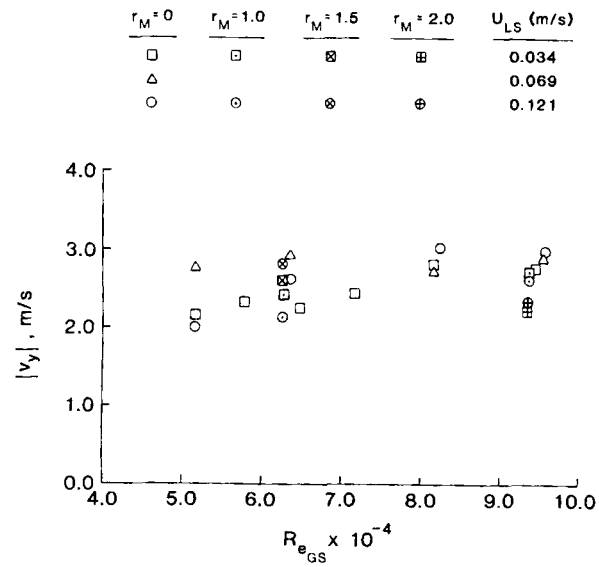

Figure 11. Dependence of average radial velocity on flow rates and radial position.

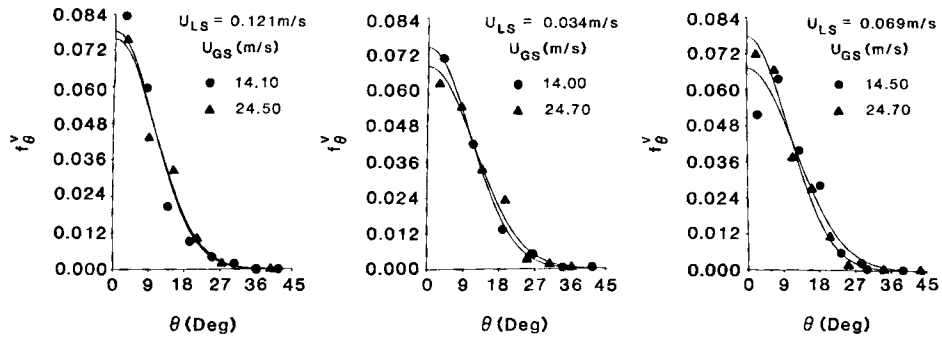

Figure 12. Experimental and theoretical angle probability density functions f_θ^v.

8.5°. The value of $\bar{\theta}_v$ obtained at other radial positions was essentially constant and equal to its value at the centerline, indicating linear trajectories of these large drops as suggested by Russel and Rogers (1972) and Whalley *et al.* (1979).

Deposition Model

Droplet trajectory

Consider a liquid spherical drop of diameter d and density ρ_l, at any arbitrary time, t, traveling in a gas of density ρ_g moving under the action the pressure gradient ∇p. The velocity vector relative to a fixed frame of reference is $\underline{v}$, for the particle. If the particle density is taken to be constant, and there is no mass transfer between the gas and the particle, then the equation of motion for the drop is:

$$\frac{d\underline{v}}{dt} = \left(\frac{1-\gamma}{\gamma}\right) g\underline{k} - \frac{3}{2}\frac{1}{\rho_l}\nabla p + \frac{3}{4}\frac{\rho_g}{d} C_D \underline{U}_S |U_S|, \qquad (21)$$

where $\underline{k}$ is the unit vector pointed upward in the vertical direction, γ is the density ratio, ρ_l/ρ_g and C_D the drag coefficient. The position vector, $\underline{x}(t)$, can be found from:

$$\frac{d\underline{x}(t)}{dt} = \underline{v}(t). \qquad (22)$$

Using a modified drag law based on experimental data of Clift and Gauvin (1971) where the gas turbulence level is taken into account, trajectories of droplets, $\underline{x}(t)$, were computed by solving the dynamic equations, Eq. 21 and 22, simultaneously, for given initial conditions, $\underline{x}(0)$, $\underline{v}(0)$. In Figure 14 typical results are presented for different droplet sizes, using the modified drag law. Different initial droplet velocities were set for each graph, a constant lateral velocity was imposed as suggested by the experimental results, and representative values for pressure drop and turbulence levels in annular flow were used.

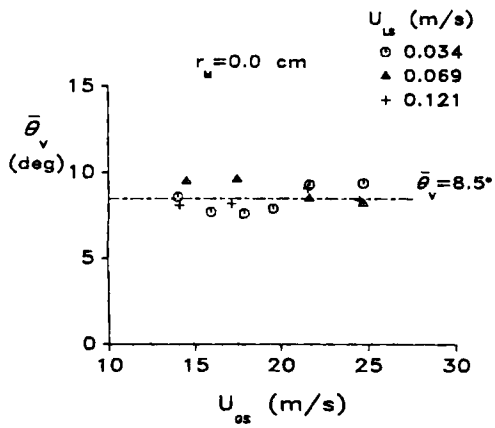

Figure 13. Experimental values of average angle $\bar{\theta}_v$ vs. U_{GS} for various values of U_{LS} at centerline.

As can be observed from these results, the droplet trajectory is almost linear. The axial and radial scales in this figure are in the same proportion as those in the experimental apparatus. This linearity can be explained by the constancy of the radial velocity and by the fact that most of the droplet acceleration is observed in the initial period of the droplet flight, when the slip velocity is extremely high.

In Figure 14, for the selected pairs of v_{z_0} and v_y the initial angles correspond to 34°, 18°, and 12°, respectively. The values of θ at the centerline differ from the initial ones, but are comparable to the angle observed over most of the droplet flight. The data also show that the angle distributions are essentially independent of radial position. This is another indication that a linear trajectory exists that is not significantly affected by the turbulent gas fluctuations.

Deposition rate of droplets

Consider any cross section of a column at a distance z_0 from the entrance, as in Figure 15, with an average area A_{z_0}. At $z > z_0$ the droplets that deposit either originate at $z < z_0$ and deposit in the distance L_D, or they are entrained in the region $z > z_0$ and also deposit in that region. The objective here is to find the mass flow rate of droplets, $W_D(L_D)$, that deposit within a distance L_D in the axial direction of the flow after crossing the cross section located at z_0.

All the droplets that contribute to $W_D(L_D)$ must pass through the cross section A_{z_0}. Thus, A_{z_0} can be viewed as a domain of droplet point sources, S_0. Each point source S_0 is located by a set of cylindrical coordinates (z_0, r, ϕ) and carries a particular volumetric flux rate of droplets $U_{S_0}(r, \phi)$.

Droplets are generated at each source with random directions and speeds. The directions are defined by the local spherical coordinates, ζ and θ, of the droplet velocity vector, $\underline{v}$, as depicted in Figure 15b. The range of the source and the droplet direction coordinates is given by:

Source Coordinates	Droplet Local Directional Coordinates
$0 \le z_0 \le L$	$0 \le \zeta \le 2\pi$
$0 \le r \le (D + 2\overline{m})/2$	$0 \le \theta \le \pi/2$
$0 \le \phi \le 2\pi$	

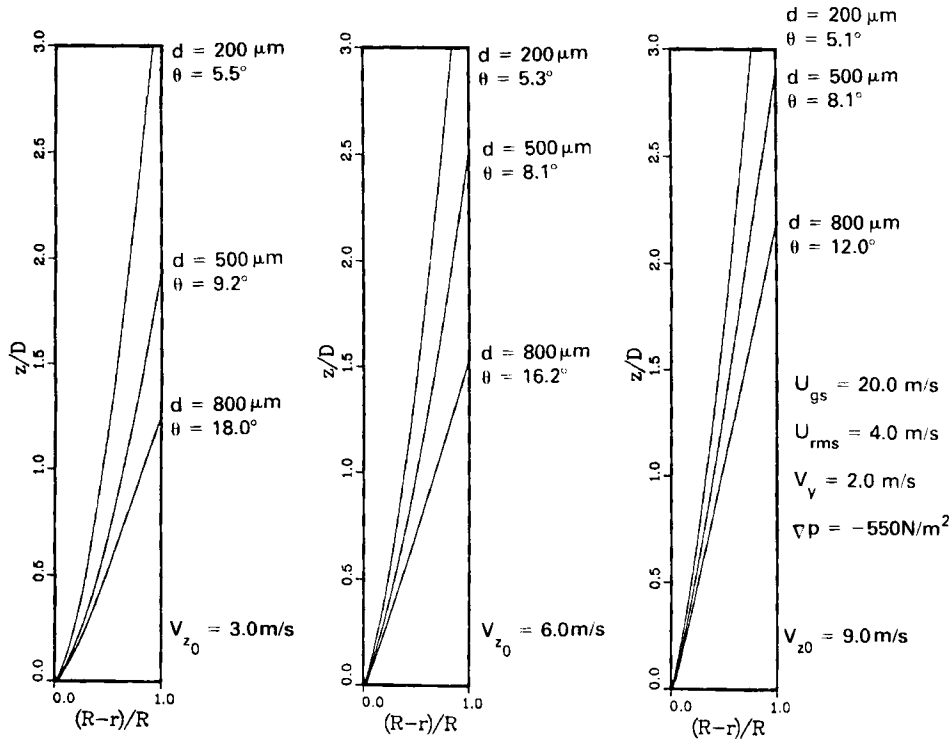

Figure 14. Droplet trajectories for various values of initial velocity $v_z(0)$.

where D is the column diameter, L is the column length, and $\overline{m}$ is the average liquid film thickness. With these new coordinates, $W_D(L_D)$ can be expressed as a surface integral:

$$W_D(L_D) = \int_{A_{z_0}} \rho_l U_{S_0}(r, \phi)\, F_D^V(r, \phi, L_D)\, dA, \qquad (23)$$

where $F_D^V(r, \phi, L_D)$ represents the volumetric fraction of the droplets generating from $S_0(r, \phi)$ that deposit within a distance L_D from the reference cross section A_{z_0}.

The function $F_D^V(r, \phi, L_D)$ can be related to the joint volume-angle probability density function $f_{\theta_t}^V$ by the following integral relationship:

$$F_D^V(r, \phi, L_D) = 1.0 - \int_0^{2\pi} \int_0^{\theta_D(r,\zeta,L_D)} f_{\theta_t}^V d\theta' d\zeta'. \qquad (24)$$

where $\theta_D(r, \zeta, L_D)$ is the angle between the axis and the line connecting the origin at $z = z_0$ and the interface at $z = z_0 + L_D$ (Figure 15).

A simple trigonometric relationship can be found between θ_D, the deposition distance L_D, and the distance, l, of the source $S_0(r, \phi)$ to the interface measured in the ζ-direction, using the premise that the drop trajectory is linear (Figure 15b):

$$\theta_D = \frac{\pi}{2} - \arctan\left(\frac{L_D}{l}\right). \qquad (25)$$

The relationship between l, r, and ζ is:

$$l = 2R_c\left\{\left(\frac{r}{R_c}\right)\cos\zeta + \sqrt{1 - \left(\frac{r}{R_c}\right)^2 + \left[\left(\frac{r}{R_c}\right)\cos\zeta\right]^2}\right\}, \qquad (26)$$

where

$$R_c = \frac{1}{2}(D + 2\overline{m}) = \frac{1}{2}D_c. \qquad (27)$$

Assuming that θ and ζ are independent variables in a statistical sense, then $f_{\theta_t}^V$ can be obtained once the individual volume-angle probability density functions, f_θ^V and f_ζ^V, are known:

$$f_{\theta_t}^V = f_\theta^V \cdot f_\zeta^V. \qquad (28)$$

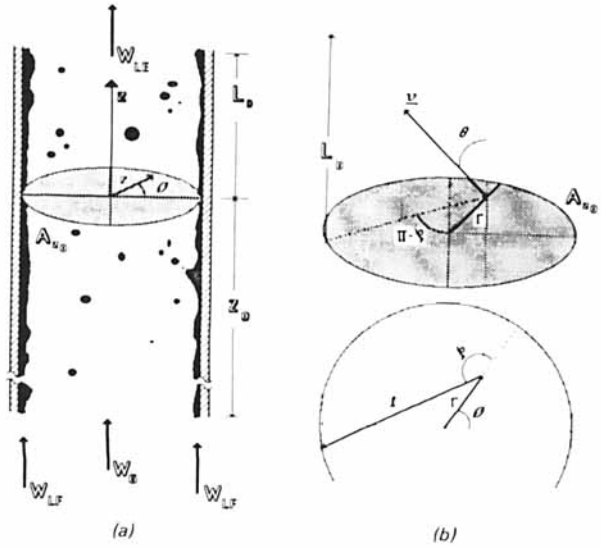

Figure 15. Droplet source characteristics.

a. Droplet source plane A_{z_0}
b. Droplet source directional coordinates.

This assumption is easily verified since droplets passing through any point source are generated from all radial directions. Furthermore, for each radial direction ζ, droplets can originate from any axial direction, θ, upstream of A_{z_0}.

It is assumed that f_ζ^V is a uniform distribution, since there is symmetry in the ζ-direction. This implies that:

$$f_\zeta^V(\zeta) = \frac{1}{2\pi}, \quad 0 \le \zeta \le 2\pi. \tag{29}$$

Substituting 29 into Eq. 28 results in:

$$f_{\theta_\zeta}^V(\theta, \zeta) = \frac{1}{2\pi} f_\theta^V(\theta). \tag{30}$$

and using this result in Eq. 24:

$$F_D^V(r, \phi, L_D) = 1.0 - \frac{1}{2\pi}\int_0^{2\pi}\int_0^{\theta_D(r,\zeta,L_D)} f_\theta^V(\theta')\, d\theta' d\zeta'. \tag{31}$$

The inner integral is F_θ^V, the volume fraction of drops moving at an angle θ. Thus:

$$F_D^V(r, \phi, L_D) = 1.0 - \frac{1}{2\pi}\int_0^{2\pi} F_\theta^V[\theta_D(r, \zeta', L_D)]\, d\zeta'. \tag{32}$$

Inserting Eq. 32 into Eq. 23 gives:

$$W_D(L_D) = \int_0^{2\pi}\int_0^{R_c} \rho_l U_{S_0}(r', \phi') r' dr' d\phi' - \frac{1}{2\pi}\int_0^{2\pi}\int_0^{R_c}\int_0^{2\pi} \rho_l U_{S_0}(r', \phi') \cdot F_\theta^V[\theta_D(r', \zeta', L_D)] r' d\zeta' dr' d\phi'. \tag{33}$$

The first integral represents the total mass flow rate, through A_{z_0}, of droplets entrained, W_{LE}. For the second integral, it will be assumed that U_{S_0} is a constant, independent of position in the plane, and given by:

$$U_{S_0}(r, \phi) = \frac{W_{LE}}{\rho_l A_{z_0}}. \tag{34}$$

This assumption is based on experimental data presented by Gill et al. (1964), who found that the drop flux profile was almost constant in the central region of the gas core. Toward the interface an increase in the liquid flux was observed, but according to the authors this resulted from the contact between the sampling probe and the surface wave liquid film.

Substituting Eq. 34 into Eq. 33 and rearranging:

$$W_D(L_D) = W_{LE}\left\{1.0 - \frac{1}{A_{z_0}}\int_0^{R_C}\int_0^{2\pi} r' F_\theta^V[\theta_D(r', \zeta', L_D)]\, d\zeta' dr'\right\}. \tag{35}$$

The expression between the braces represents the mass fraction of droplets that cross A_{z_0} and deposit within a distance L_D. This term will be referred to as $X(L_D)$, and Eq. 35 becomes:

$$W_D(L_D) = W_{LE} X(L_D). \tag{36}$$

Therefore the rate of deposition of drops, $W_D(L_D)$, can be computed given the rate of flow of entrained drops W_{LE} and an expression for F_θ^V. This can be calculated from a fit to the measurement of f_θ^V.

A model for f_θ^V

The axial directional angle θ is a one-sided variable extending from 0 to $\pi/2$. In order to introduce a symmetrical density function, a new angle, η, is defined:

$$|\eta| = \theta; \quad -\frac{\pi}{2} \le \eta \le \frac{\pi}{2}. \tag{37}$$

This variable contains the information about the relative direction of movement of the droplet with respect to the axis of the column, and can be associated with a Gaussian distribution:

$$f_\eta^V(\eta) = \frac{1}{\sqrt{2\pi} s_\eta} \exp\left[-\frac{1}{2}\left(\frac{\eta - \bar{\eta}}{s_\eta}\right)^2\right], \tag{38}$$

where $\bar{\eta}$ is the average value of η and s_η is its standard deviation. Since symmetry exists under rotation of ζ, then $\bar{\eta} = 0$. Hence:

$$f_\eta^V(\eta) = \frac{1}{\sqrt{2\pi} s_\eta} \exp\left[-\frac{1}{2}\left(\frac{\eta}{s_\eta}\right)^2\right]. \tag{39}$$

In order to obtain f_θ^V from Eq. 39, it is necessary to apply the transformation of variables given by Eq. 37. The two density functions are related through (Papoulis, 1965):

$$f_\theta^V(\theta) = 2 f_\eta^V(\eta), \tag{40}$$

and placing Eq. 39 into Eq. 40 finally gives:

$$f_\theta^V(\theta) = \frac{2\delta^*}{\sqrt{\pi}} \exp\left[-(\delta^*\theta)^2\right], \quad \delta^* = \frac{1}{\sqrt{2} s_\eta}. \tag{41}$$

This is a single-parameter model that can be tested against experimentally measured values of f_θ^V. The relationship between the parameter δ^* and the average angle, $\bar{\theta}_V$, can be obtained through:

$$\bar{\theta}_V = \int_0^\infty \theta' f_\theta^V(\theta')\, d\theta' = \frac{2\delta^*}{\sqrt{\pi}}\int_0^\infty \theta' \exp\left[-(\delta^*\theta')^2\right] d\theta' = \frac{1}{\delta^*\sqrt{\pi}}, \tag{42}$$

and the standard deviation, s_V, is related to δ^* through:

$$s_V = (\overline{\theta_V^2} - \bar{\theta}_V^2)^{1/2} = \left(\frac{1}{2\delta^{*2}} - \frac{1}{\pi\delta^{*2}}\right)^{1/2} = \frac{1}{\delta^*}\left(\frac{\pi - 2}{2\pi}\right)^{1/2}. \tag{43}$$

The experimental density functions, f_θ^V, were obtained from the simultaneous measurement of the droplet diameter and two velocity components, obtaining θ through Eq. 22. The model of f_θ^V proposed by Eq. 41 was tested against the experimental density functions, and a value of δ^* that minimizes the χ^2 statistics was chosen. Figure 12 shows the experimental density functions

(points) against the theoretical model (curve) for different gas and liquid rates at the center position. Generally good agreement is observed.

Final form of the deposition model

The distribution function F_θ^V in Eq. 35 can be computed using f_θ^V as defined by Eq. 41:

$$F_\theta^V(\theta_D) = \int_0^{\theta_D} f_\theta^V(\theta')\, d\theta' = \int_0^{\theta_D} \frac{2\delta^*}{\sqrt{\pi}} \exp\left[-(\delta^*\theta')^2\right] d\theta' = \operatorname{erf}(\delta^*\theta_D). \quad (44)$$

Thus:

$$X(L_D) = \frac{W_D(L_D)}{W_{LE}} = 1.0 - \frac{1}{A_{z_0}} \int_0^{R_c} \int_0^{2\pi} r' \operatorname{erf}\left[\delta^*\theta_D(r', \zeta', L_D)\right] d\zeta'\, dr', \quad (45)$$

which is the final form of the deposition model determined by the geometry of the column, A_{z_0}, the gas core flow area, R_c, and the droplet volume angle distribution parameter, δ^*, which is found from f_θ^V.

In Figure 16 the values of $X(L_D)$, the fraction of the droplets crossing any plane that are deposited in a distance L_D downstream, are plotted against the dimensionless distance, L_D/D, for different values of $\bar{\theta}_V$. The distance the droplets travel inside the gas core before depositing their mass can now be examined. For $\bar{\theta}_V \approx 9°$, 50% of the mass of droplets deposits within a distance equivalent to three tube diameters, while at a distance of 18 diameters only 10% of the initially entrained mass is still traveling in the gas core. Since the experimentally measured values of $\bar{\theta}_V$ varied narrowly between 8° and 10°, the deposition distribution function is almost constant. This is especially so since $X(L_D)$ is not strongly dependent on $\bar{\theta}_V$ for $\bar{\theta}_V > 8°$, as can be

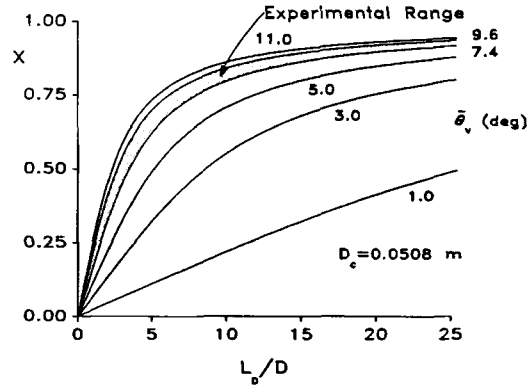

Figure 16. Fractional deposition X vs. deposition length L_D for various values of $\bar{\theta}_V$.

observed in Figure 16. The function $X(L_D)$ only gives partial information on the deposition transfer. The goal is to find the total rate of deposition that provides knowledge of the rate of droplet entrainment in equilibrium annular flow.

Droplet Deposition Rates

Since the mass deposition flux N_D is constant, the total mass flow rate $W_D^T(L_D)$ over a distance L_D is:

$$W_D^T(L_D) = N_D \pi D_c L_D. \quad (46)$$

In the limit as L_D goes to zero, the rate of reentrainment over the length L_D is negligible compared to the rate at which droplets pass the plane A_{z_0}. Thus in the limit, $L_D \to 0$, and at any arbitrary position, z, along the tube:

$$N_D = \frac{1}{\pi D_c} \frac{d}{dL_D} W_D(L_D)\big|_{L_D \to 0}, \quad (47)$$

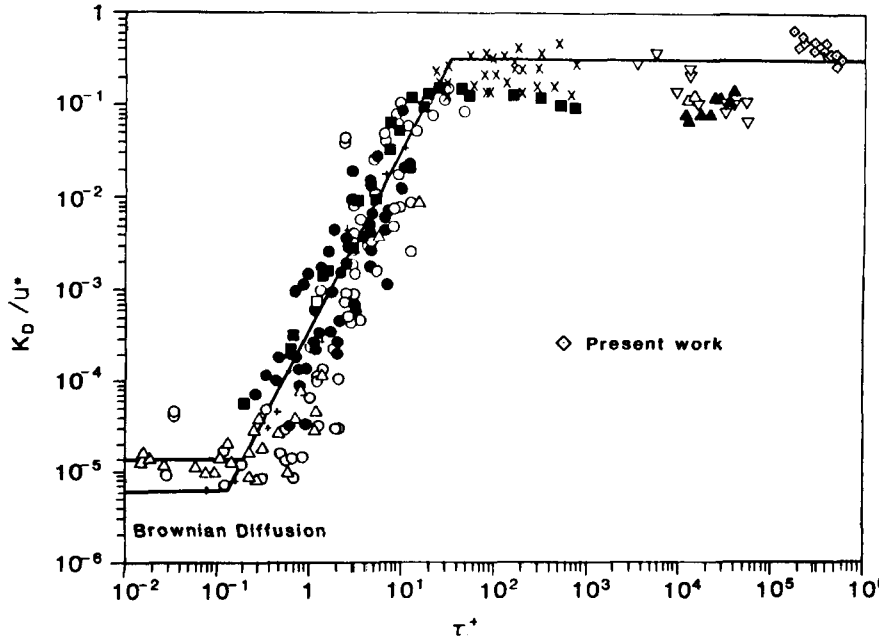

Figure 17. Deposition rates of published data (McCoy and Hanratty, 1977), plus experimental values from present work.

Placing Eq. 36 in Eq. 47:

$$N_D = \frac{W_{LE}}{\pi D_c} \frac{d}{dL_D} X(R_c, \delta^*)|_{L_D \to 0}. \tag{48}$$

Thus, once W_{LE}, D_c, and δ^* or $\bar{\theta}_V^*$ are obtained from experiments, the values of N_D can be computed. Furthermore, N_D can be related to the mass transfer coefficient, K_D, which is commonly reported in the literature:

$$N_D = K_D \frac{\rho_g W_{LE}}{W_G}, \tag{49}$$

where ρ_g is the density of the gas core and W_G is the gas mass flow rate. Then, K_D relates to X, through K_D/U_{GS}, as:

$$\frac{K_D}{U_{GS}} = \frac{D_c}{4} \frac{d}{dL_D} X(R_c, \delta^*)\Big|_{L_D \to 0}, \tag{50}$$

where U_{GS} is average gas velocity over the pipe cross section. For small film thickness ($D \gg \overline{m}$), D_c can be approximated by D. It can be seen that $4K_D/D_c U_{GS}$ is simply the slope of the curves in Figure 16 at the origin.

Comparison of deposition rates with experimental data

The comparison with other data is made by plotting the dimensionless quantity K_D/u^*, where u^* is the gas frictional velocity, vs. a dimensionless particle relaxation time τ^+, defined as:

$$\tau^+ = \frac{1}{18} \frac{\rho_l}{\rho_g} \left(\frac{\rho_g u^* d}{\mu_g} \right)^2, \tag{51}$$

where d, the particle diameter, is taken as the arithmetic mean average $\bar{d}_{10}$. The values of K_D/u^* and τ^+ as calculated from Eq. 50 with the experimental data are plotted in Figure 17, together with previous data reviewed by McCoy and Hanratty (1977). The values of u^* used here were obtained from the experimental correlation developed in the next section.

It can be observed that the values found in the present work are consistent with other data reported for large values of τ^+, a region where the inertia of the large particles is controlling. For smaller values of τ^+ a strong dependence of K_D/u^* with τ^+ is observed, revealing a strong influence of the turbulence diffusion. However, the inclusion of the data of the present work reinforces the idea (McCoy and Hanratty, 1977) that for $\tau^+ > 10^2$ there exists an independence of K_D/u^* from τ^+. The somewhat smaller values of K_D/u^* for some of the other data are probably due to the fact that the values of u^* used were overestimated, since the total pressure gradient used to calculate u^* included droplet acceleration.

Cousins and Hewitt (1968) present experimental results on X vs. L_D in vertical annular flow. Figure 18 shows three curves of their measured X vs. L_D for different pipe sizes and flow rates. These experiments were designed to avoid reentrainment. The single-parameter model represented by Eq. 45 was used to fit the data. In each case a value of δ^* was found by a least-squares technique. The curves of Figure 18 represent Eq. 45, which shows excellent agreement with the data over the full range of L_D values. This result is superior to predictions of Hutchinson *et al.* (1971) with these same data. In their work a diffusion process was used as the basic mechanism.

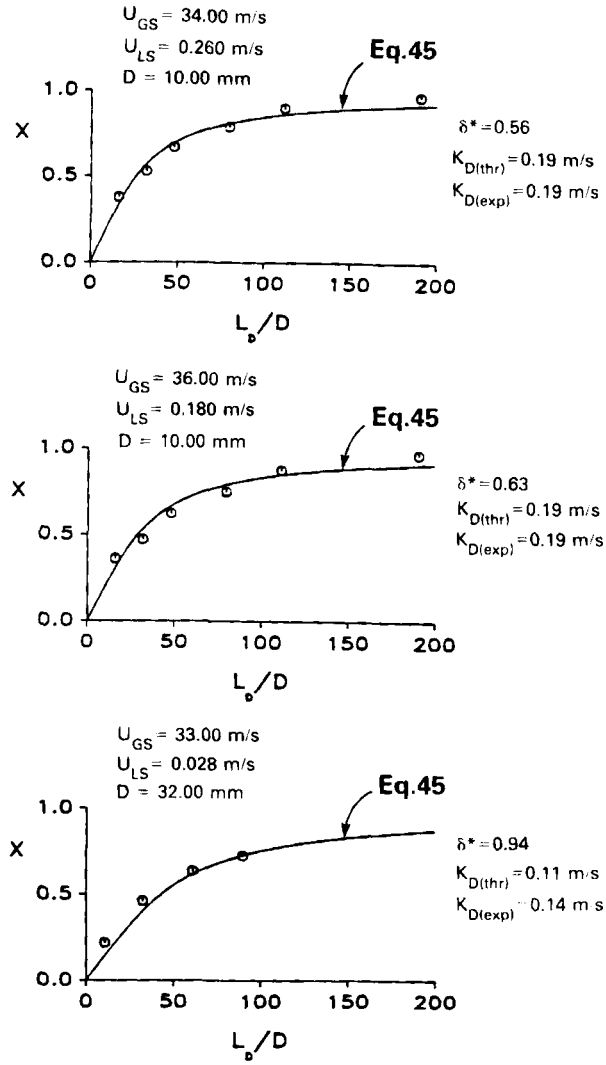

Figure 18. Experimental curves, X vs. L_D/D.
⊙, Cousins and Hewitt (1968)
—— Theoretical curves from best fit of Eq. 45

This result is additional evidence that in annular flow, because of the drops' large size droplet inertia controls droplet dynamics. That is, linear trajectories exist rather than the tortuous trajectories predicted by diffusion-type models.

Pressure Drop Due to Entrainment and Interfacial Shear

With this deposition model, along with the momentum balance given by Eq. 6, it is now possible to compute the contribution of each momentum transfer mechanism to the measured total pressure drop. Given ∇p, W_{LE}, $\overline{m}$, $\bar{\theta}_V$, and $\bar{v}_z$ for each input gas and liquid rate, α_c is computed from Eq. 11, which provides ∇p_G (Eq. 9). N_D is calculated using Eq. 48, v_i from Eq. 12, and then ∇p_E from Eq. 10. Finally, ∇p_f is then obtained by difference using Eq. 7.

Data are tabulated by Lopes (1984) for $\bar{\theta}_V$ and $\bar{v}_z$. Zabaras (1985) has obtained a full range of data on W_{LE}, ∇p, and $\overline{m}$ (Figures 7 and 19). These data were used to compute each com-

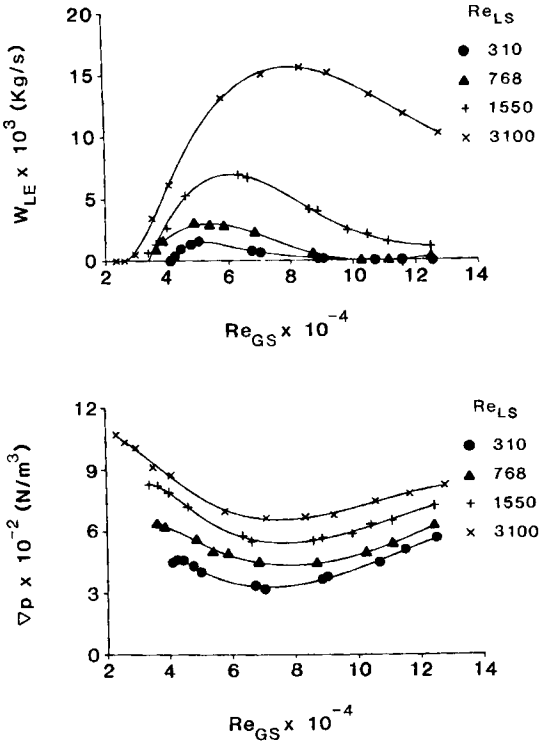

Figure 19. Experimental values of ∇p_T, W_{LE} vs. Re_{GS} (Zabaras, 1985).

ponent of the pressure gradient; the results appear in Figure 20. For the lowest liquid rate, it is observed that the entrainment and gravitational pressure gradient have a negligible contribution to ∇p. The pressure gradient results primarily from the friction of the gas core against the wavy liquid surface. As Re_{LS} increases, ∇p_E increases. At the largest experimental value of Re_{LS}, ∇p_E can actually be the dominant term over a range of Re_{GS}. ∇p_G is always negligible for these conditions.

This behavior gives a partial explanation for the existence of a minimum in the ∇p vs. Re_{GS} curve. At low gas rates the liquid film transports most of the liquid, as can be concluded from Figure 19. As the gas rate is increased for a fixed liquid rate, the amount of liquid transported by the film is reduced and the entrainment increases until a maximum in entrainment is achieved. It is hypothesized that the process of liquid transport in the form of drops can be accomplished at a lower energy dissipation rate, since the high shear stresses experienced by the liquid in the film do not exist. As the gas rate increases the fraction entrained decreases, more liquid is carried by the film, and the rate of energy dissipation increases again.

A variety of correlations have been proposed for the interfacial friction factor, f_i, few with any physical basis. In general, the friction factor is calculated directly from the total measured pressure gradient and empirically correlated. From Figure 20 it is clear that only a component of this measured pressure drop is related to the interfacial shear. It is now possible to evaluate f_i using only that component of pressure drop due to shear, ∇p_I. The interfacial friction factor is thus:

$$f_i = \frac{\tau_i}{\frac{1}{2}\rho_g(U_G - v_i)^2} = \frac{(D - 2\overline{m})\nabla p_I}{2\rho_g(U_G - v_i)^2}. \tag{52}$$

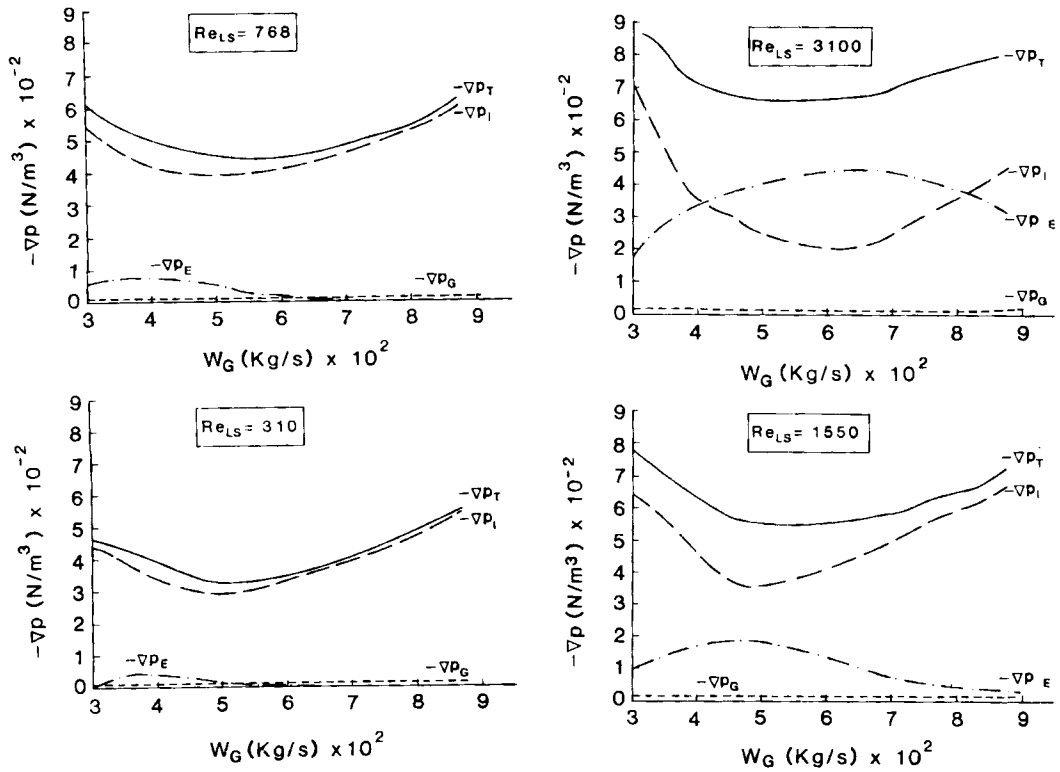

Figure 20. Pressure gradient terms in Eq. 11 vs. W_G for various values of U_{LS}.

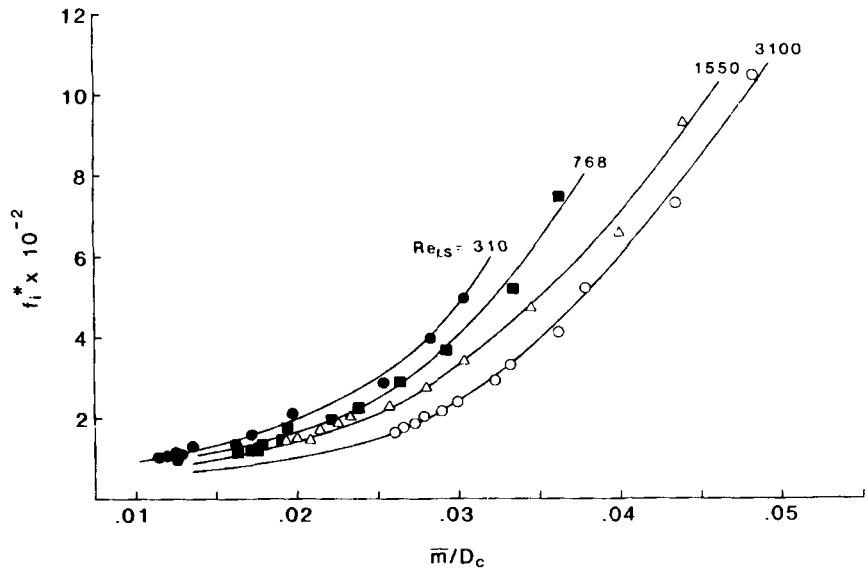

Figure 21. Friction factor values f_i^* evaluated with entrainment contribution vs. $\overline{m}/D_c$ for various values of Re_{LS}.

where U_G is the average gas velocity in the gas core, given by:

$$U_G = \frac{4W_G}{\pi(D - 2\overline{m})^2}. \tag{53}$$

Wallis (1968), Moeck (1970), Hughmark (1972), Henstock and Hanratty (1975), and Barathan (1978) have all suggested that f_i is uniquely dependent on $\overline{m}/D$. These correlations ignore the role of momentum transfer of the droplets in determining the pressure drop. Following the procedure of these authors, f_i was calculated using the measured value of ∇p. For $\nabla p_f = \nabla p$ in Eq. 52, the results are presented in Figure 21, where the friction factor calculated this way is designated by f_i^*. It is evident that a unique relation between f_i^* and $\overline{m}/D$ does not really exist and there is a significant dependence on liquid rates.

Correlations based on $\overline{m}/D$ suggest that the interface presents a fully developed rough interface to the gas. However, when f_i^* is plotted against Re_G, as in Figure 22, it is clear that the curves describe transition type roughness. Here:

$$Re_G = \frac{\rho_g(U_G - v_i)D_c}{\mu_g}, \tag{54}$$

where all these quantities can be determined unambiguously.

True values of the interfacial friction factor f_i, calculated from ∇p_f rather than the total measured value of pressure gradient, appear in Figure 23. The result seems quite striking. Here f_i is independent of liquid rate and displays the transition roughness.

Further studies will be necessary before the generality of this curve can be established. However, the important role of the entrainment and redeposition process on the observed pressure gradient is clearly established.

Acknowledgment

This work was made possible by financial support from the Nuclear Regulatory Commission and the National Science Foundation.

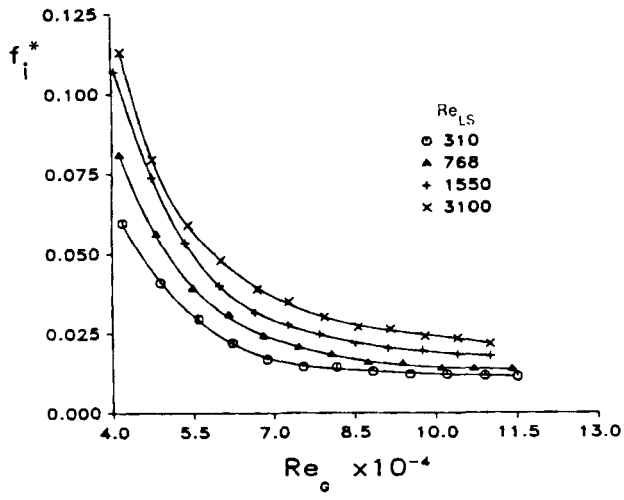

Figure 22. Friction factor values f_i^* evaluated with entrainment contribution vs. Re_G for various values of Re_{LS}.

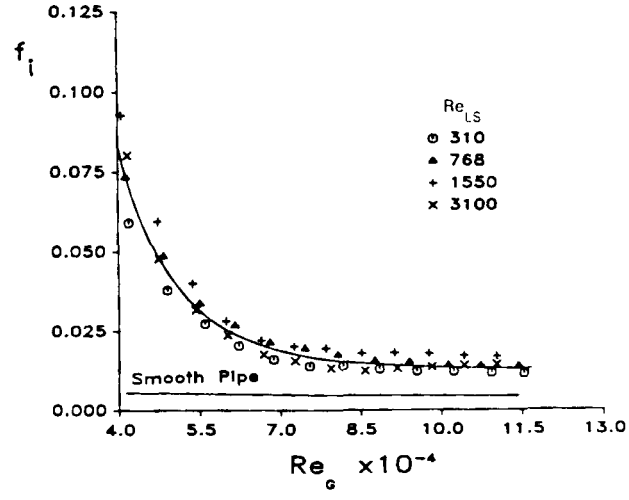

Figure 23. Friction factor values f_i evaluated without entrainment contribution vs. Re_G for various values of Re_{LS}.

Notation

$\underline{A}$ = vector area
A_c = gas core cross-sectional area
A_{z_0} = reference cross-sectional area at position z_0
$\underline{B}$ = body force vector per unit mass
B_z = body force component in the z direction per unit mass
C_D = droplet drag coefficient
d = droplet diameter
d_{max} = maximum droplet diameter
$\bar{d}_{10}$ = arithmetic mean diameter
$\bar{d}_{32}$ = Sauter mean diameter
D = column diameter
D_c = diameter of gas core
f_i = interfacial friction factor, Eq. 52
f_i^* = interfacial friction factor, Eq. 52 where $\nabla p_I = \nabla p$
f_{v_z} = number-axial velocity probability density function
f_θ^V = volume-angle probability density function
$f_{\theta\zeta}^V$ = joint volume-angles θ and ζ probability density function
f_ζ^V = volume-angle ζ probability density function
f_η^V = volume-angle η probability density function
f_y = grating frequency in the y direction
f_z = grating frequency in the z direction
F_d^N = number-diameter probability distribution function
F_d^V = volume-diameter probability distribution function
F_D^V = volumetric fraction of droplets function, Eq. 23
F_θ^V = volume-angle θ probability distribution function
g = gravity acceleration
$\underline{k}$ = unit directional vector in the z direction
K_D = mass transfer coefficient, Eq. 49
l = distance from the wall of droplet source S_0
L_D = axial distance for droplet deposition
$\bar{m}$ = average liquid film thickness
m_{max} = maximum liquid film thickness
N_D = mass flux rate of depositing droplets on the liquid film
N_E = mass flux rate of entrained droplets from the liquid film
p = local dynamic pressure
r = radial coordinate
r_M = radial coordinate of measurement point
R = column radius
R_c = radius of gas core
Re_G = gas Reynolds number, Eq. 54
Re_{GS} = gas Reynolds number $(\rho_g U_{GS} D)/\mu_g$
Re_{LS} = liquid Reynolds number $(\rho_l U_{LS} D)/\mu_l$
s = viewing slit gap size
s_F = fringe spacing
s_η = standard deviation of η
S_C = enclosing area of gas core control region
S_L = lateral interfacial area
S_R = slip ratio, Eq. 16
S_{R_0} = slip ratio at centerline
S_T = transverse area
S_0 = droplet source at A_{z_0}
t = time
$\underline{T}$ = local traction force vector
T_z = local traction force vector z component
u^* = friction velocity of gas phase $(\tau_i/\rho_g)^{1/2}$
u_{rms} = root-mean-square gas turbulent velocity
U_G = average axial velocity of gas in the gas core
U_{G_0} = axial velocity of gas at centerline
U_{GS} = superficial gas velocity $4W_G/(\rho_g \pi D^2)$
U_{LS} = superficial liquid velocity $4W_L/(\rho_l \pi D^2)$
U_{LF} = liquid film average velocity
U_S = gas slip velocity, $U_G - \bar{v}_z$
U_{S_0} = volumetric flux rate of droplets at source S_0
$\underline{v}$ = droplet velocity vector
$\underline{v}_i$ = interfacial liquid velocity
v_y = droplet lateral or radial velocity
$|\bar{v}_y|$ = droplet number-average radial velocity
v_z = droplet axial velocity
$\bar{v}_z$ = droplet number-average axial velocity
V_C = volume of gas core control region
V_L = volume of liquid in the control region
V_G = volume of gas in the control region
$W_D(L_D)$ = mass flow rate of droplets depositing within a distance L_D
$W_D^T(L_D)$ = total mass flow rate of depositing droplets within a distance L_D
W_G = gas mass flow rate
W_L = liquid mass flow rate
W_{LE} = mass flow rate of entrained droplets
W_{LF} = liquid film mass flow rate
$\underline{x}$ = particle trajectory vector
$X(L_D)$ = mass fraction of droplets that deposit within a distance L_D
z_0 = axial coordinate of cross reference section

Greek letters

α_c = gas core void fraction
γ = density ratio, ρ_l/ρ_g
δ^* = parameter of probability distribution function of droplet angle, Eq. 41
Δp = pressure difference between any two points in opposite tops of control volume at a distance L_D
ζ = droplet axial directional angle coordinate
η = modified droplet angle variable, Eq. 37
θ = droplet axial directional angle coordinate, Eq .22
θ_D = deposition angle, Eq. 24
$\bar{\theta}_V$ = volume-average droplet angle
μ_f = fluid viscosity
μ_g = gas phase viscosity
μ_l = liquid phase viscosity
ρ = phase density
ρ_g = gas phase density
ρ_l = liquid phase density
τ^+ = dimensionless drop relaxation time, Eq. 51
τ_i = interfacial shear stress
τ_{PT} = droplet passage time
ϕ = angular cylindrical coordinate
∇p = total pressure gradient
∇p_E = entrainment pressure gradient
∇p_G = gravitational pressure gradient
∇p_I = interfacial pressure gradient

Literature cited

Andreussi, P., and B. J. Azzopardi, "Droplet Deposition and Interchange in Annular Two-Phase Flow," *Int. J. Multiphase Flow*, **9**, 681 (1983).

Azzopardi, B. J., "Drop Sizes in Annular Two-Phase Flow," *Exper. in Fluids*, **3**, 53 (1985).

Barathan, D., "Air-Water Countercurrent Annular Flow in Vertical Tubes," Elec. Power Res. Inst. Report, EPRI NP-786 (1978).

Clift, R., and W. H. Gauvin, "Motion of Entrained Particles in Gas Streams," *Can. J. Chem. Eng.*, **49**, 430 (1971).

Cousins, L. B., and G. F. Hewitt, "Liquid Phase Mass Transfer in Annular Two-Phase Flow: Droplet Deposition and Liquid Entrainment," UKAEA Report AERE-R5657 (1968).

Dukler, A. E., and P. G. Magiros, "Entrainment and Pressure Drop in Concurrent Gas Liquid Flow; Distribution and Momentum Effects," *Dev. in Mechanics*, **1**, 532 (1962).

Gill, L. E., G. F. Hewitt, and P. M. C. Lacey, "Sampling Probe Studies of the Gas Core in Annular Two-Phase Flow. II: Studies of the Effect of the Phase Flow Rates on Phase and Velocity Distributions," *Chem. Eng. Sci.*, **19**, 665 (1964).

Henstock, W. H., and T. J. Hanratty, "Interfacial Drag and Film Height in Annular Flows," *AIChE J.*, **21**, 990 (1975).

Hughmark, G. A., "Notes on Transfer in Turbulent Pipe Flow," *AIChE J.*, **18**, 1072 (1972).

Hutchinson, P., G. F. Hewitt, and A. E. Dukler, "Deposition of Liquid or Solid Dispersions from Turbulent Gas Streams: A Stochastic Model," *CES*, **26**, 419 (1971).

Lopes, J. C. B., "Droplet Sizes, Dynamics and Deposition in Vertical Annular Flow," Ph.D. Diss. Univ. Houston, Texas (1984).

McCoy, D. D., and T. J. Hanratty, "Rate of Deposition of Droplets in Annular Two-Phase Flow," *Int. J. Multiphase Flow*, **3**, 319 (1977).

Moeck, E. O., and J. W. Stachiewicz, "A Droplet Interchange Model for Annular-Dispersed, Two-Phase Flow," *Int. J. Heat Mass Trans.*, **15**, 637 (1972).

Papoulis, A., *Probability, Random Variables, and Stochastic Processes*, McGraw-Hill, New York (1965).
Russel, T. W., and R. W. Rogers, "Droplet Behavior in Horizontal Gas-Liquid Flow," *AICHE Symp. Multiphase Flow in Pipes*, Dallas (Feb., 1972).
Schlichting, H., *Boundary-Layer Theory*, McGraw-Hill, New York (1979).
Semiat, R., and A. E. Dukler, "Simultaneous Measurements of Size and Velocity of Bubbles or Drops: A New Optical Technique," *AIChE J.*, **27**, 148 (1981).
Swithenbank, J., J. M. Beer, D. S. Taylor, D. Abbot, and G. C. Mccreath, "A Laser Diagnostic Technique for the Measurement of Droplet and Particle Size Distributions," *Prog. Astronautics Aeronautics*, **53**, 421 (1977).
Tatterson, D. F., "Rates of Atomization and Drop Size in Annular Two-Phase Flow," Ph.D. Diss., Univ. Illinois (1975).
Wallis, G. B., "Discussion of Paper by Paleev and Fillipovich," *Int. J. Heat Mass Trans.*, **11**, 783 (1968).
Whalley, P. B., G. F. Hewitt, and J. W. Terry, "Photographic Studies of Two-Phase Flow Using a Parallel Light Technique," UKAEA Report AERE-R9398 (1979).
Wilkes, N. S., B. J. Azzopardi, and I. Willets, "Drop Motion and Deposition in Annular Two-Phase Flow," *Proc. Nuclear Reactor Thermal-Hydraulics*, Am. Nuclear Soc., **1**, 202 (1983).
Zabaras, G., "Studies of Vertical Annular Gas-Liquid Flows," Ph.D. Diss., Univ. Houston, Texas (1985).

Manuscript received Sept. 23, 1985, and revision received Jan. 13, 1986.